FRONTIERS OF PHYSICS

RESEARCH ARTICLE
Volume 21 / Issue 9 / 093202 / 2026

Quantum signatures of mixed classical phase space in Floquet systems

Ke Li, Xiao-Fu Han, Sheng-Chang Li†

MOE Key Laboratory for Nonequilibrium Synthesis and Modulation of Condensed Matter, Shaanxi Province Key Laboratory of Quantum Information and Quantum Optoelectronic Devices, and School of Physics, Xi'an Jiaotong University, Xi'an 710049, China
Corresponding author. E-mail: †scli@xjtu.edu.cn
Received November 4, 2025; accepted January 5, 2026

© Higher Education Press 2026

ABSTRACT

Identifying quantum chaos in Floquet systems with mixed classical phase spaces requires robust experimentally accessible signatures. We investigate the time-averaged quantum Fisher information (QFI) and the fidelity out-of-time-ordered correlator (FOTOC) of continuous periodically driven systems. We uncover two distinct power-law scalings of the time-averaged QFI with respect to system size: the standard quantum limit and the Heisenberg limit. These scalings correspond to initial states localized in the regular and chaotic regions of the classical phase space, respectively. Remarkably, we show that the time-averaged FOTOC can accurately identify the transition from mixed phase space to fully chaotic sea (at a critical driving strength $B_x \approx 5.3$) as verified by the maximum Lyapunov exponent. The results suggest that both time-averaged QFI and FOTOC can be used as excellent quantum signatures for probing mixed phase-space structures and our adopted protocol for measuring the FOTOC eliminates the need for time-reversal operations. This work establishes a practical framework for investigating quantum chaos in Floquet systems, bridging theoretical insights with experimental applications.

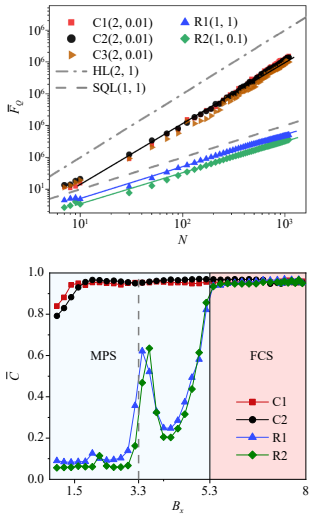

Keywords mixed phase space, quantum chaos, quantum Fisher information, fidelity out-of-time-ordered correlator

1 Introduction

Quantum chaos, which reveals the profound connections between quantum systems and classical chaos [1–3], has attracted considerable attention for understanding the complex behavior of chaotic systems. In contrast to classical chaos, which is characterized by exponential sensitivity to initial conditions, the distance between two quantum states remains unchanged due to unitary evolution. This fundamental issue makes identifying quantum chaos particularly challenging in periodically driven systems (i.e., Floquet systems) that exhibit mixed classical phase spaces. Floquet systems [4, 5] serve as ideal platforms for exploring quantum chaos, where the rich physics has potential applications in quantum information processing and condensed matter physics. Paradigm models include the kicked top [6, 7], the kicked rotor [8–10], and the kicked Harper model [11, 12], among others. However, most established models employ delta-kick driving, which simplifies the temporal structure of driving fields and may not fully capture the dynamical richness of continuously driven many-body systems. The detection of quantum chaos in Floquet systems with mixed classical phase space remains an open problem, as traditional

https://doi.org/10.15302/frontphys.2026.093202

indicators, such as energy-level statistics [13, 14] and eigenstate properties [15, 16], are insufficient for effectively identifying the coexistence of regular and chaotic dynamics. In addition, how initial states localized in mixed phase space affect the dynamics of multipartite entanglement — characterized by the quantum Fisher information (QFI) — is a fundamental issue with significant implications for the fields of quantum chaos and quantum information.

Now, it is found that QFI serves as an effective tool for quantifying how rapidly information about an initial state dissipates over time. The time-averaged QFI [17] can assess sensitivity to perturbations in chaotic systems and detect measurement-induced phase transitions in collective spin models [18, 19]. In the context of chaotic quantum metrology [20], QFI has been observed experimentally in a harmonically driven Bose–Josephson system [21]. Interestingly, QFI is directly related to the out-of-time-order correlator (OTOC) when specific operators are chosen in its construction. Recently, OTOC has been widely used to quantify quantum phase transitions [22, 23], many-body localization [24–26], and holographic duality [27]. Theoretical studies have further established its equivalence with the thermal average of the Loschmidt echo [28], thereby bridging the gap between quantum chaos and quantum information scrambling [29]. Moreover, OTOCs have been measured experimentally in systems such as trapped ions [30] and nuclear magnetic resonance quantum simulators [31]. Recent works have uncovered key links between classical chaos and quantum OTOCs [32–34]. While these works focused on OTOC dynamics in globally chaotic or single-particle systems, detecting quantum chaos in Floquet systems with mixed phase spaces — where regular and chaotic dynamics coexist — remains an open challenge. Notably, the fidelity OTOC (FOTOC), a specific OTOC variant, is recognized as a critical indicator of quantum chaos in systems with mixed classical phase spaces, particularly for distinguishing chaotic from integrable dynamics. Although FOTOC's exponential growth may arise from either quantum chaos or classical saddle points, their long-term behaviors differ significantly [35]. This is crucial not only for understanding the quantum-to-classical transition but also for its emerging applications in entanglement-enhanced quantum metrology.

In this context, we reconstruct the structure of the mixed classical phase space in a continuously driven two-mode Bose–Einstein condensate (BEC) model using time-averaged QFI and FOTOC. This model exemplifies a many-body Floquet system under continuous periodic driving, offering a rich testbed beyond kicked models. We identify two distinct power-law scalings of the QFI: the standard quantum limit and Heisenberg limit, which correspond to initial states localized in regular islands and chaotic regions, respectively. This contrasts with the universal power-law relation between the time-averaged QFI and particle number N reported for chaotic initial states in kicked-top systems [18]. Our finding highlights a key difference between discrete-kick and continuous-drive dynamics in mixed phase spaces, and offers a straightforward method to distinguish the eigenstates of chaotic systems, shedding light on the fundamental problem in quantum chaos [36]. We further demonstrate that the time-averaged FOTOC not only quantifies the chaotic sensitivity to initial conditions but also identifies the critical driving strength (i.e., $B_x \approx 5.3$) for the transition from a mixed phase space to a fully chaotic regime. Our results indicate that both the time-averaged QFI and FOTOC can serve as quantum signatures for probing mixed phase spaces in continuously driven many-body Floquet systems.

The rest of the paper is organized as follows. In Section 2, we introduce a continuous periodically driven two-mode BEC system and its description. In Section 3, we demonstrate the structure of the mixed classical phase space of the Floquet system. In Section 4, we explore two quantum signatures of the mixed phase space: the time-averaged QFI and FOTOC. Finally, Section 5 gives a brief discussion and summary.

2 Model

We consider a periodically driven two-mode BEC described by the Bose–Josephson model. The time-dependent Hamiltonian (with $\hbar = 1$) is given by [21]

$$\hat{H}(t) = B_z \hat{J}_z + \frac{c}{N}\hat{J}_z^2 + a(t)\hat{J}_x, \tag{1}$$

where the collective spin angular momentum operators are defined as $\hat{J}_x = (\hat{a}_1^\dagger \hat{a}_2 + \hat{a}_2^\dagger \hat{a}_1)/2$, $\hat{J}_y = (\hat{a}_2^\dagger \hat{a}_1 - \hat{a}_1^\dagger \hat{a}_2)/2i$, and $\hat{J}_z = (\hat{a}_2^\dagger \hat{a}_2 - \hat{a}_1^\dagger \hat{a}_1)/2$. Here, $\hat{a}_{1,2}$ and $\hat{a}_{1,2}^\dagger$ denote the bosonic annihilation and creation operators for atomic modes labeled 1 and 2, respectively. The total spin is $J = \frac{N}{2}$ with N being the total particle number. The parameters B_z, c, and $a(t)$ represent the static longitudinal field strength, the atomic interaction strength, and the driving field describing the coupling between the two modes, respectively. Given that various driving protocols have been explored, including kicked pulses and quasi-Floquet drives [37], we adopt a harmonic driving of the form $a(t) = B_x \cos \omega t$, where B_x and ω denote the driving amplitude and frequency of the transverse field, respectively.

To study the quantum dynamics, we employ a spin-coherent state (SCS) as the initial state,

$$|\theta, \phi\rangle_J = \sum_{\mu=-J}^{J} \sqrt{\binom{2J}{J+\mu}} \left(\cos\frac{\theta}{2}\right)^{J-\mu} \left(\sin\frac{\theta}{2}\right)^{J+\mu} \times \mathrm{e}^{\mathrm{i}(J+\mu)\phi} |\mu\rangle, \tag{2}$$

where θ and ϕ are the polar and azimuthal angles, respectively, and $|\mu\rangle$ stands for the eigenstate of $\hat{J}_z$. The mean spin direction is given by $(S_x, S_y, S_z) = (\sin\theta\cos\phi, \sin\theta\sin\phi, \cos\theta)$. The classical phase space spanned by (S_z, ϕ) can be directly mapped to the quantum SCS $|\theta, \phi\rangle_J$, where $S_z = \cos\theta$ represents the population imbalance between two atomic modes. This correspondence is geometrically illustrated on the Bloch sphere [38], with the south pole (i.e., $S_z = -1$ or $\theta = \pi$) corresponding to the spin-down state $|\downarrow\rangle \equiv |-J\rangle$, where all particles occupy the lower-energy mode.

3 Mixed classical phase space

The total particle number N of the Floquet system described by Eq. (1) is conserved. In the mean-field limit $N \to \infty$, the operators $\hat{J}_l$ $(l = x, y, z)$ reduce to classical variables S_l, forming a Bloch vector constrained to the unit sphere with conserved norm [39], i.e., $\hat{a}_j \approx a_j = |a_j|\exp(\mathrm{i}\phi_j)$ and $\hat{a}_j^\dagger \approx a_j^* = |a_j|\exp(-\mathrm{i}\phi_j)$ $(j = 1, 2)$ with $|a_1|^2 + |a_2|^2 = N$. As a result, the population imbalance $S_z = (|a_1|^2 - |a_2|^2)/N$ and the relative phase $\phi = \phi_1 - \phi_2$ between two atomic modes form a pair of classical canonical variables, and the classical Hamiltonian $H(t)$ reads [40]

$$H(t) = \frac{c}{2}S_z^2 - B_z S_z + B_x \cos\omega t\sqrt{1 - S_z^2}\cos\phi. \tag{3}$$

The corresponding Hamilton equations, determining the motions in classical phase space spanned by (S_z, ϕ), are given by

$$\frac{\mathrm{d}\phi}{\mathrm{d}t} = cS_z - B_z - \frac{B_x S_z \cos\omega t}{\sqrt{1 - S_z^2}}\cos\phi, \tag{4}$$

$$\frac{\mathrm{d}S_z}{\mathrm{d}t} = B_x \cos\omega t\sqrt{1 - S_z^2}\sin\phi. \tag{5}$$

To characterize the global phase-space dynamics of the classical system, we construct Poincaré sections by stroboscopically sampling the phase-space trajectories (S_z, ϕ) at integer multiples of the driving period $T = 2\pi/\omega$, i.e., $t = nT$ with $(n = 1, 2, \cdots)$. A maximum of 500 points in the (S_z, ϕ) phase space are shown in Fig. 1 for the parameter set $(\omega, B_x, B_z, c) = (2\pi, 1.5, \pi/2, 10)$, where each point is plotted in black. The Poincaré section exhibits the coexistence of regular islands and chaotic sea, which is clear evidence of the mixed phase space.

Classical chaos is characterized by the exponential divergence of nearby trajectories, reflected in a positive maximum Lyapunov exponent (MLE),

$$\lambda_{\max} = \lim_{m\to\infty}\frac{1}{mT}\sum_{n=1}^{m}\ln\frac{||(\delta S_x(nT), \delta S_y(nT), \delta S_z(nT))||}{||(\delta S_x(0), \delta S_y(0), \delta S_z(0))||}, \tag{6}$$

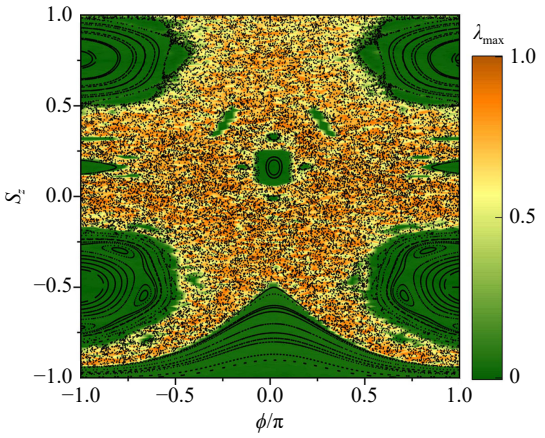

Fig. 1 Comparison between Poincaré section (black points) and MLE $\lambda_{\max}$ (colors) for different initial states. We have set $c = 10$, $B_x = 1.5$, and $B_z = \pi/2$.

where $\delta S_{x,y,z}(nT) = |S'_{x,y,z}(nT) - S_{x,y,z}(nT)|$ denotes the component-wise deviations between two trajectories at time $t = nT$, and $||\cdot||$ denotes the Euclidean vector norm. In numerical simulations, one needs to reset the perturbed trajectory to be close to the unperturbed trajectory, namely, back to the initial deviation, at the beginning of each period, while keeping its stretching direction unchanged. In our numerical calculations, we set $\delta S_z(0) = 10^{-5}$ and evolve the system from various initial trajectories (S_z, ϕ) over the interval $t \in [0, 500T]$ to ensure the convergence of the $\lambda_{\max}$. The values of $\lambda_{\max}$ for various initial conditions are shown in Fig. 1, where the color gradient quantifies the magnitude of $\lambda_{\max}$. One can see that $\lambda_{\max}$ is larger in the chaotic sea (predominantly orange, with $\lambda_{\max} > 0$), and vanishes in the regular islands (dark green, with $\lambda_{\max} \approx 0$). This correspondence verifies the existence of a mixed phase space, comprising both regular and chaotic dynamics.

4 Quantum signatures of mixed phase space

4.1 Time-averaged QFI

For a mixed quantum state $\hat{\rho} = \sum_\lambda p_\lambda|\lambda\rangle\langle\lambda|$, such as a thermal ensemble [41], the QFI is given by [42, 43]

$$F_Q(t) = 2\sum_{\lambda,\lambda'}\frac{(p_\lambda - p_{\lambda'})^2}{p_\lambda + p_{\lambda'}}|\langle\lambda|\hat{O}|\lambda'\rangle|^2, \tag{7}$$

where $\hat{O}$ is a generic Hermitian operator, and $|\lambda\rangle$ is an energy eigenstate with occupation probability p_λ. The model in Eq. (1) describes a spin-J system composed of N spin-1/2 particles (or qubits), where the collective spin operators are defined as $\hat{J}_l = \sum_{j=1}^N \sigma_l^{(j)}/2$, with $\sigma_l^{(j)}$ $(l = x, y, z)$ denoting the Pauli matrices for the j-th particle or qubit. For a pure quantum state $\hat{\rho} = |\psi_t\rangle\langle\psi_t|$,

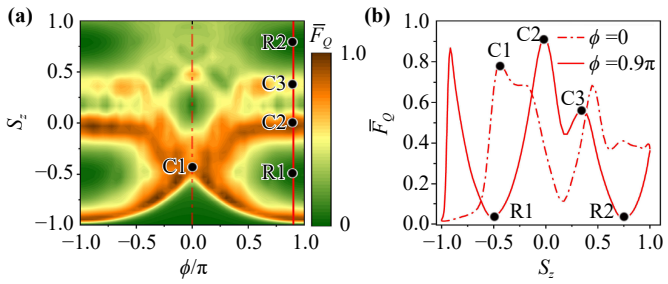

Fig. 2 **(a)** Distribution of the rescaled time-averaged QFI $\overline{F}_Q$ (rescaled by $\overline{F}_{Q,\max} \approx 5000$) in the initial state space parameterized by (S_z, ϕ). **(b)** $\overline{F}_Q$ as a function of S_z (curves for $\phi = 0$ and $\phi = 0.9\pi$ correspond to the dot-dashed and solid lines in (a), respectively). Solid black points marked by C1, C2, C3, R1, and R2, denote the initial SCSs $|\theta, \phi\rangle_J = |0.35\pi, 0\rangle$, $|0.49\pi, 0.9\pi\rangle$, $|0.62\pi, 0.9\pi\rangle$, $|0.33\pi, 0.9\pi\rangle$, and $|0.77\pi, 0.9\pi\rangle$, respectively. Parameters: $N = 200$ and $\tau = 100T$; other parameters match those in Fig. 1.

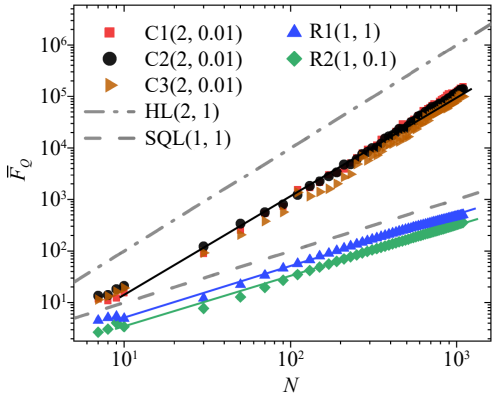

Fig. 3 Time-averaged QFI $\overline{F}_Q$ as a function of N for different initial SCSs. Solid lines marked by (η, ζ) denote fits to $\overline{F}_Q = \zeta N^\eta$ with ζ and η being two fitting constants. The fitting exponents (with standard errors) are: $\eta_{C1} = 1.976 \pm 0.017$, $\eta_{C2} = 1.891 \pm 0.016$, $\eta_{C3} = 1.866 \pm 0.023$, $\eta_{R1} = 0.972 \pm 0.007$, and $\eta_{R2} = 0.988 \pm 0.007$. The gray dash-dot and dashed lines represent the Heisenberg limit (HL) and standard quantum limit (SQL), respectively. We have set $\tau = 100T$ and the initial states correspond to those in Fig. 2.

e.g., the ground state of a given Hamiltonian, the QFI simplifies to a connected correlation function that is readily computable or measurable. Consequently, Eq. (7) reduces to

$$F_Q(t) = 4(\Delta\hat{O})^2 = 4(\langle\psi_t|\hat{O}^2|\psi_t\rangle - \langle\psi_t|\hat{O}|\psi_t\rangle^2), \tag{8}$$

where $\Delta\hat{O}$ denotes the standard deviation of the observable $\hat{O}$ with respect to the state $|\psi_t\rangle$. In many quantum systems, the $\hat{J}_z$ operator represents an experimentally accessible quantity, particularly in cold-atom experiments where particle population imbalances can be measured with high precision [44, 45]. Therefore, we choose $\hat{O} = \hat{J}_z$ to construct the QFI.

Note that chaotic dynamics often induce strong fluctuations in time-dependent quantities. To smooth out these fluctuations and better capture the system's statistical properties over long time scales, we introduce the time-averaged QFI, defined as [18]

$$\overline{F}_Q \equiv \lim_{\tau\to\infty} \frac{1}{\tau} \int_0^\tau \mathrm{d}t F_Q(t). \tag{9}$$

We numerically investigate the distribution of $\overline{F}_Q$ in the initial state space parameterized by (S_z, ϕ), as depicted in Fig. 2(a). We set $\tau = 100T$ to ensure convergence of the time-averaged quantities and to reliably capture the system's long-term statistical behavior. To clearly compare its relative strength across regions, $\overline{F}_Q$ is rescaled by its maximum value ($\overline{F}_{Q,\max} \approx 5000$) over the entire parameter space. Clearly, the values of $\overline{F}_Q$ depend strongly on whether the initial state lies in a classically chaotic or regular region: states in chaotic regions (see C1, C2, and C3) exhibit significantly larger $\overline{F}_Q$, whereas those in regular regions (see R1 and R2) yield smaller values. This behavior closely follows the MLE distribution shown in Fig. 1, indicating a strong correlation between the time-averaged QFI and the structure of the mixed classical phase space.

The QFI has been employed to reveal the role of chaos in parameter estimation, showing that initial states in chaotic seas exhibit superior QFI dynamics compared to those in regular islands [21]. We further investigate the dependence of $\overline{F}_Q$ on S_z for specific values of ϕ to reveal its dynamical behavior under different initial state parameters. Figure 2(b) shows $\overline{F}_Q$ as a function of S_z for two representative azimuthal angles, i.e., $\phi = 0$ and $\phi = 0.9\pi$, highlighting five characteristic initial SCSs: two in regular regions (R1: $|0.33\pi, 0.9\pi\rangle$ and R2: $|0.77\pi, 0.9\pi\rangle$) and three in chaotic regions (C1: $|0.35\pi, 0\rangle$, C2: $|0.49\pi, 0.9\pi\rangle$, and C3: $|0.62\pi, 0.9\pi\rangle$). It is evident that the values for C1, C2, and C3 are significantly larger than those for R1 and R2, demonstrating the enhancement of quantum metrology sensitivity facilitated by classical chaos. It should be emphasized that whether the initial states are located in the regular or chaotic region is related to the choice of parameters. In Fig. 2 we set $(\omega, B_x, B_z, c) = (2\pi, 1.5, \pi/2, 10)$, if a different set of parameters is used, the initial states (e.g., R1 and R2) in the regular region may enter the chaotic sea.

Figure 3 shows the dependence of $\overline{F}_Q$ on the particle number N for different initial states, highlighting distinct scaling behaviors. The scaling behaviors follow a power-law,

$$\overline{F}_Q = \zeta N^\eta, \tag{10}$$

where ζ and η are fitting constants. The fitted exponents for the selected initial states are: $\eta_{C1} = 1.976 \pm 0.017$, $\eta_{C2} = 1.891 \pm 0.016$, $\eta_{C3} = 1.866 \pm 0.023$, $\eta_{R1} = 0.972 \pm 0.007$,

and $\eta_{\mathrm{R2}} = 0.988 \pm 0.007$. This scaling difference originates from the distinct phase-space mixing characteristics. For initial states in the regular region (i.e., R1 and R2), $\overline{F}_Q$ remains below the standard quantum limit (SQL) with $\eta = 1$, which represents the fundamental bound for classical systems. In contrast, for states in the chaotic region (i.e., C1, C2, and C3), $\overline{F}_Q$ surpasses the SQL but is below the Heisenberg limit (HL) with $\eta = 2$, the ultimate bound for quantum precision. Compared to previous studies that employed QFI [21], the time-averaged QFI used here smooths out dynamical fluctuations and extracts robust statistical behavior. The ability of the time-averaged QFI to accurately recover the SQL and HL scalings stems from its reflection of the distinct Krylov-space structures governing quantum dynamics in chaotic versus regular regions [18]. Remarkably, the power-law dependence holds robustly across system sizes, remaining valid even for small N. The QFI can serve as a key indicator for assessing measurement precision in quantum systems under chaotic dynamics. Unlike the instantaneous QFI [46, 47], which probes momentary sensitivity, the time-averaged QFI integrates dynamics over extended time scales, offering a powerful tool to characterize scaling differences between chaotic and regular states as system size varies.

4.2 Time-averaged FOTOC

For chaotic systems, the FOTOC $C(t)$ typically exhibits exponential growth characterized by the classical Lyapunov exponent. The short-time exponential growth of the FOTOC in chaotic regions is intrinsically linked to the classical Lyapunov exponent. Theoretically, for times $t \ll T$, the FOTOC can be approximated as $C(t) \sim \mathrm{e}^{2\lambda t}$, where λ denotes the classical Lyapunov exponent [48, 49]. Beyond offering deep insights into quantum chaos dynamics, $C(t)$ also has the practical advantage of experimental accessibility and relative ease of measurement. It is defined as follows:

$$C(t) = 1 - \langle \hat{W}^{\dagger}(t)\hat{\rho}_0^{\dagger}\hat{W}(t)\hat{\rho}_0\rangle, \tag{11}$$

where $\hat{W}(t)$ is a Hermitian or unitary operator in the Heisenberg picture at time t, and $\hat{\rho}_0 = |\theta,\phi\rangle\langle\theta,\phi|_J$ denotes the projector onto the initial SCS $|\theta,\phi\rangle_J$. Here $\langle\cdot\rangle$ denotes the quantum expectation value with respect to the initial SCS $|\theta,\phi\rangle_J$. For a pure initial state $\hat{\rho}_0$, this expression simplifies significantly [50] to

$$C(t) = 1 - |\langle \hat{W}(t)\rangle|^2, \tag{12}$$

where $|\langle \hat{W}(t)\rangle|^2$ is experimentally measurable, for example by means of Ramsey interferometry or spin-projection techniques in cold-atom systems without requiring complex time-reversal control sequences. The adopted protocol [44, 50] enables direct evaluation through the use of only forward evolution, serving as a critical and experimentally accessible metric for characterizing the exponential growth behavior associated with quantum chaos [51]. Therefore, this approach substantially enhances the experimental feasibility of detecting quantum chaos in Floquet-driven systems. Here, $\hat{W}(t) = \hat{U}^{\dagger}(t,0)\hat{W}\hat{U}(t,0)$ denotes the time-evolved form of $\hat{W} \equiv \hat{W}(0)$. The time-evolution operator $\hat{U}(t,0)$ is given by

$$\hat{U}(t,0) = \hat{\mathcal{T}} \exp\left(-\mathrm{i}\int_0^t \hat{H}(t')\,\mathrm{d}t'\right), \tag{13}$$

where $\hat{\mathcal{T}}$ is the time-ordering operator [21].

We use the rotation operator with an infinitely small parameter ϵ to construct the $C(t)$. It is defined by

$$\hat{W} \equiv \hat{W}_{\epsilon}(\theta,\phi) = \mathrm{e}^{-\mathrm{i}\epsilon \boldsymbol{n}(\theta,\phi)\cdot\boldsymbol{J}}, \tag{14}$$

where $\boldsymbol{n}(\theta,\phi) = (\sin\theta\cos\phi, \sin\theta\sin\phi, \cos\theta)^{\mathrm{T}}$ denotes the axis of rotation and $\boldsymbol{J} = (\hat{J}_x, \hat{J}_y, \hat{J}_z)^{\mathrm{T}}$ is the vector of angular momentum operators. For $\epsilon \ll 1$, we have $\hat{W}_{\epsilon}(\theta,\phi) \approx 1 - \mathrm{i}\epsilon\boldsymbol{n}\cdot\boldsymbol{J} + \mathcal{O}(\epsilon^2)$, which leads to $F(t) \approx 1 - \epsilon^2(\Delta(\boldsymbol{n}\cdot\boldsymbol{J}))^2$ and consequently yields $C(t) \approx \epsilon^2(\Delta(\boldsymbol{n}\cdot\boldsymbol{J}))^2$. This establishes a direct connection with QFI defined in Eq. (8) when we choose $\hat{O} = \boldsymbol{n}\cdot\boldsymbol{J} = \hat{J}_z$,

$$C(t) \approx \frac{\epsilon^2}{4} F_Q(t). \tag{15}$$

The quantitative relationship between the FOTOC and QFI [42] reveals their utility in probing quantum chaos via the system's response to initial perturbations. Notably, the time-averaged values of FOTOC and QFI also satisfy the relation (15), as numerically confirmed in Appendix A.

The time-averaged FOTOC $\overline{C}$ is written as

$$\overline{C} = \lim_{\tau\to\infty} \frac{1}{\tau}\int_0^{\tau} \mathrm{d}t C(t). \tag{16}$$

We numerically investigate the $\overline{C}$, in the mixed phase space for $N = 200$ and $\epsilon = \pi/40$, which are optimized to clearly distinguish chaotic features (see Appendix B). Figure 4(a) illustrates the distribution of $\overline{C}$ over the initial state space (S_z, ϕ), revealing a clear separation between chaotic and regular regions. Similar to the time-averaged QFI shown in Fig. 2(a), $\overline{C}$ also exhibits higher values in chaotic regions and lower values in regular regions, further confirming the correspondence between quantum and classical chaos. Although both the time-averaged QFI and FOTOC serve as quantum chaos indicators, they capture fundamentally different aspects: $\overline{F}_Q$ reflects intrinsic quantum fluctuations and determines metrological precision limits, whereas the $\overline{C}$ measures the dynamical response to perturbations. This explains why $\overline{F}_Q$ [see Fig. 2(a)] and $\overline{C}$ [see Fig. 4(a)] exhibit different behaviors in the positive S_z region, with $\overline{C}$ showing better agreement with the classical MLE (see

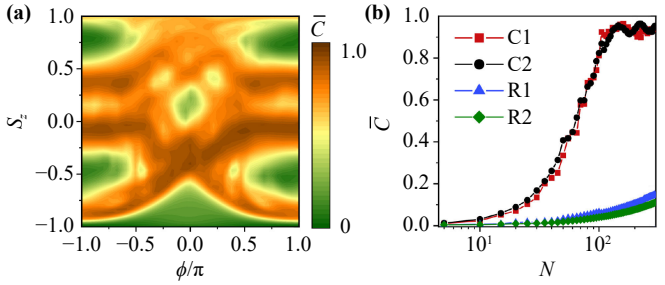

Fig. 4 **(a)** Distribution of the time-averaged FOTOC $\overline{C}$ in initial state space parameterized by (S_z, ϕ). **(b)** $\overline{C}$ as a function of N for different initial states. We have set $\epsilon = \pi/40$ and other parameters are the same as those in Fig. 2.

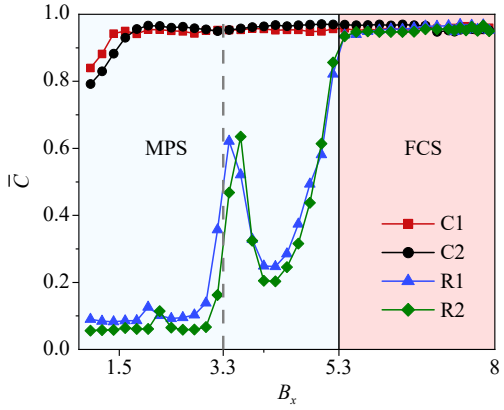

Fig. 5 Time-averaged FOTOC $\overline{C}$ as a function of B_x for four different initial SCSs. Dashed vertical line marks $B_x \approx 3.3$ where $\overline{C}$ increases sharply for the initial states R1 and R2, while solid vertical line denotes $B_x \approx 5.3$ where $\overline{C}$ becomes saturated, which gives the signal of the transition from MPS (light blue area on the left) to FCS (pink area on the right). We have set $N = 200$ and $\epsilon = \pi/40$; other parameters match those in Fig. 2.

Fig. 1). Figure 4(b) shows the dependence of $\overline{C}$ on N for different initial states. One can see that initial states in chaotic regions (i.e., C1 and C2) lead to rapid growth and saturation of $\overline{C}$, whereas states in regular regions (i.e., R1 and R2) exhibit persistent low-amplitude oscillations. These results highlight the effectiveness of the $\overline{C}$ as an indicator of classical chaos and reinforce its utility as a robust experimental signature for probing mixed phase spaces. We also numerically investigate the Husimi-Q distribution and observe distinct dynamical evolution characteristics for different initial states in the mixed phase space (see Appendix C), which the time-averaged FOTOC effectively captures.

Figure 5 shows $\overline{C}$ as a function of B_x for different initial SCSs, with parameters chosen in accordance with Ref. [21]. The corresponding Poincaré sections illustrate a transition from a mixed phase space (MPS) to a fully chaotic sea (FCS) as B_x increases. Our results demonstrate that $\overline{C}$ effectively traces this transition. Specifically, for the initial states R1 and R2, $\overline{C}$ saturates when B_x exceeds a critical value, i.e., $B_x \approx 5.3$ (indicated by the vertical solid line), reflecting the MPS-FCS transition in agreement with the classical phase-space structure analysis (see Appendix D). For a more comprehensive visualization of the fully chaotic sea, the distributions of $\overline{F}_Q$ and $\overline{C}$ in this regime are presented in Appendix E (Fig. A6). Note that there is a pseudo-critical point at $B_x \approx 3.3$ (indicated by the dashed vertical line), where the $\overline{C}$ for the initial states R1 and R2 exhibits a sharp increase with B_x, signaling the onset of the MPS-to-FCS transition within an extremely narrow parameter window. For comparison, the $\overline{C}$ for the initial states C1 and C2 remains saturated as B_x varies. Our findings prove that $\overline{C}$ can serve as an effective diagnostic tool for detecting quantum chaos.

5 Discussion and conclusion

In summary, we have developed robust quantum signatures to characterize mixed classical phase spaces within continuously driven Floquet systems, based on an analysis of the time-averaged QFI and FOTOC. Our findings reveal a fundamental connection between classical phase-space structures and the quantum dynamics of the harmonically driven Bose–Josephson model. The time-averaged QFI exhibits two distinct power-law scalings with respect to the system size N. Initial states within chaotic regions conform to the HL ($\eta = 2$), while those in regular regions follow the SQL ($\eta = 1$). The scaling behaviors remain consistent across varying system sizes, serving as a universal diagnostic tool for identifying quantum chaos in mixed phase spaces. Furthermore, the time-averaged FOTOC provides a clear marker for the transition between regular and chaotic dynamics. It accurately determines the critical driving strength, approximately $B_x \approx 5.3$, at which the system shifts from MPS to FCS, a finding validated by the MLE. Notably, our proposed protocol eliminates the necessity of time-reversal operations, thereby substantially enhancing its experimental viability.

The two-mode Bose–Josephson model can be effectively realized using a two-mode BEC, in which atoms are confined in two hyperfine levels [52, 53]. The atom–atom interaction strength c can be adjusted via Feshbach resonance [54, 55]. The driven term $a(t)$ can be implemented by applying a time-modulated magnetic field. The FOTOC defined in Eq. (12) is measurable without time reversal, enhancing its feasibility in experiments with modern quantum control techniques [50]. The scaling of the time-averaged QFI can be extracted from population measurements of $\hat{J}_z$, a routine procedure in atom-interferometry setups [42, 43]. Our work not only provides theoretical signatures of mixed phase-space chaos but also suggests a practical route for experimental verification

in the synthetic quantum systems such as trapped ions, superconducting circuits, or atomic ensembles.

Our findings advance the understanding of quantum-classical correspondence in driven systems and offer practical tools for detecting quantum chaos, with implications for both fundamental studies and applications in related fields of quantum metrology and simulation.

Declarations The authors declare that they have no competing interests and there are no conflicts.

Acknowledgements This work was supported by the National Natural Science Foundation of China (NSFC) (Grants Nos. 12375019 and 11974273).

Appendix A: Connection between time-averaged QFI and FOTOC

According to the relationship (15) between the FOTOC and QFI obtained under the condition of a small perturbation angle $\epsilon \ll 1$, the relationship between the time-averaged FOTOC and QFI can naturally be derived as follows:

$$\overline{C} \approx \frac{\epsilon^2}{4}\overline{F}_Q. \tag{A1}$$

Figure A1 presents a comparison between the time-averaged FOTOC (triangles) and the rescaled time-averaged QFI (solid line). As shown in Fig. A1, the two quantities tend to coincide as the perturbation angle decreases (e.g., from $\epsilon = 0.05$ to $\epsilon = 0.001$), validating the correctness of Eq. (A1). Additionally, for extremely small perturbation angles, the time-averaged FOTOC (or QFI) alone reflects the structure of the mixed phase space: in the regular region, $\overline{C}$ (or $\overline{F}_Q$) is approximately zero (dips in Fig. A1), whereas in the chaotic region, $\overline{C}$ (or $\overline{F}_Q$) assumes finite values (peaks in Fig. A1).

Appendix B: Dynamics of FOTOC for quantum chaos

Figure A2 shows the time evolution of the FOTOC $C(t)$ for different initial states in the mixed phase space. For chaotic initial states (e.g., C1, red curve), $C(t)$ rapidly grows and saturates near 1, whereas for regular states (e.g., R1, blue curve), it exhibits low-amplitude oscillations. This highlights the sensitivity of FOTOC dynamics to the underlying phase-space structure, paving the way for its application in detecting quantum chaos. We further investigate the time evolution of $C(t)$ for different particle numbers N and perturbation angles ϵ, with the initial state chosen in the chaotic region (i.e., C1 $|0.35\pi, 0\rangle$). For a fixed N, $C(t)$ rapidly saturates with time [e.g., $N = 2$ in Fig. A3(a)]. As N increases, the saturation value approaches unity, indicating that smaller N significantly suppresses the visibility of quantum chaotic behavior. Figure A3(b) shows the time evolution of $C(t)$ for different values of ϵ, demonstrating that smaller ϵ also suppresses signatures of chaotic dynamics. Our results uncover that both small system sizes and weak perturbations reduce the visibility of measurable quantum chaos indicators. Therefore, in the main text, we use $N = 200$ and $\epsilon = \pi/40$ to maximize the visibility of chaotic features when computing the FOTOC.

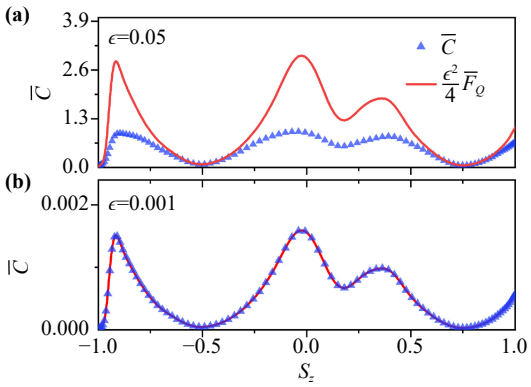

Fig. A1 Time-averaged FOTOC $\overline{C}$ (triangles) as functions of S_z for **(a)** $\epsilon = 0.05$ and **(b)** $\epsilon = 0.001$. For comparison, the rescaled time-averaged QFI $\frac{\epsilon^2}{4}\overline{F}_Q$ is shown as a solid line. Parameters are set as $\phi = 0.9\pi$, $N = 200$, and $\tau = 100T$.

Appendix C: Husimi-Q distribution of quantum state evolution

The Husimi-Q distribution is a quasiprobability distribution that effectively represents quantum states in phase space. By visualizing high-dimensional quantum states, it offers clear insights into quantum phenomena like uncertainty and coherence, thus serving as a useful tool in studies of quantum chaos [5, 56]. For a pure quantum state $\hat{\rho} = |\psi_t\rangle\langle\psi_t|$ at time t, the Husimi-Q distribution is

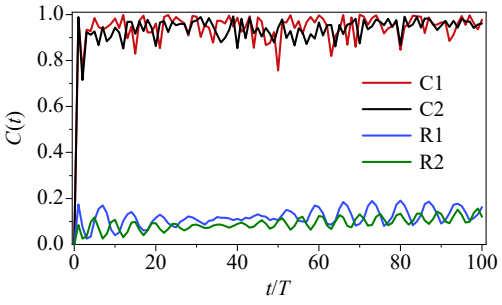

Fig. A2 Time evolution of FOTOC $C(t)$ for different initial states. The curves (from top to bottom) correspond to the initial SCSs: C1 (red), C2 (black), R1 (blue), and R2 (green). We have set $\epsilon = \pi/40$ and other parameters are the same as those in Fig. 2.

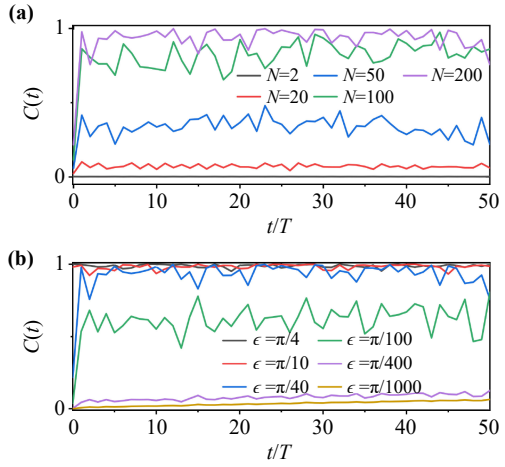

Fig. A3 Time evolution of FOTOC $C(t)$ for the initial SCS C1 for **(a)** different particle numbers N (fixed $\epsilon = \pi/40$) and **(b)** different perturbation angles ϵ (fixed $N = 200$). In (a), the curves (from top to bottom) are: $N = 200$ (purple), 100 (green), 50 (blue), 20 (red), and 2 (gray). In (b), the curves (from top to bottom) are: $\epsilon = \pi/4$ (gray), $\pi/10$ (red), $\pi/40$ (blue), $\pi/100$ (green), $\pi/400$ (purple), and $\pi/1000$ (yellow).

$$Q(\theta,\phi) = \frac{2J+1}{4\pi}\langle\theta,\phi|\hat{\rho}|\theta,\phi\rangle_J, \tag{C1}$$

where $|\theta,\phi\rangle_J$ is the SCS and $(2J+1)/4\pi$ is the normalization factor.

Figure A4 displays the Husimi-Q distributions of the time-evolved states for various initial SCSs, revealing notable differences in the evolution of states from chaotic sea to regular island. For initial states in chaotic regions (C1 and C2), the Husimi-Q distributions spread and diffuse over time, reflecting sensitivity to initial conditions, a hallmark of chaotic dynamics. In contrast, for initial states in regular regions (R1 and R2), the distributions stay localized and rotate around the z-axis on the Bloch sphere, indicating stable, periodic motion. Our findings highlight the distinct dynamical behaviors of chaotic and regular trajectories in mixed phase space, clearly visualizing the evolution of quantum states.

Appendix D: MLE analysis of MPS-FCS transition

To quantify the transition from MPS to FCS, we numerically calculate the MLE for classical trajectories with varying driven strength B_x and different initial states. The system parameters are set to be the same as in Fig. 2, i.e., $c = 10$ and $B_z = \pi/2$. Figure A5 shows that near the pseudo-critical point $B_x \approx 3.3$ (indicated by a dashed vertical line), localized regular islands (deep blue regions with $\lambda_{\max} = 0$) emerge in the mixed phase space. This marks the onset of the MPS-to-FCS transition within an extremely narrow parameter window. The

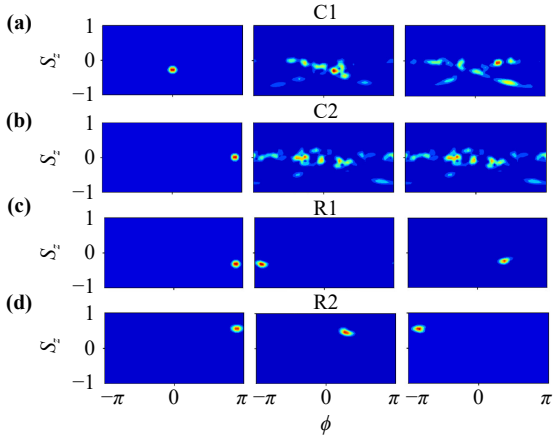

Fig. A4 Time evolution of Husimi-Q distribution (for each row, from left to right, $t = 0$, $20T$, and $50T$) for different initial SCSs: **(a)** C1 (the first row), **(b)** C2 (the second row), **(c)** R1 (the third row), and **(d)** R2 (the forth row).

pseudo-critical point at $B_x \approx 3.3$ may originate from a resonance between the driving energy B_x and the intrinsic energy $\frac{c}{2} - B_z \approx 3.4$ of the undriven system. This resonance causes the driving term to effectively couple to the system's internal modes, locally destabilizing regular orbits and forming isolated chaotic regions (deep blue islands in Fig. A5). As B_x increases further, the phase space becomes dominated by a fully chaotic sea (red regions with $\lambda_{\max} \geq 1$), and no regular islands remain for $B_x > 5.3$, indicating a definitive MPS-to-FCS transition. Notably, near the parameter values corresponding to the two transitions described above, we observe a sudden increase and a saturation signal in the time-averaged

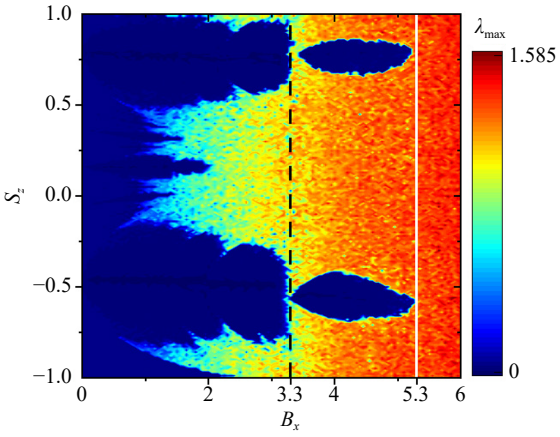

Fig. A5 MLE $\lambda_{\max}$ as a function of driving strength B_x for different initial states (S_z, ϕ). The left vertical line denotes the pseudo-critical point (i.e., $B_x \approx 3.3$) at which the transition signal from MPS to FCS (extremely narrow range) occurs for the first time and the right vertical line identifies the critical point (i.e., $B_x \approx 5.3$) at which the transition occurs for the second time. We set $\phi = 0.9\pi$ (corresponding to the solid line in Fig. 2(a)), $c = 10$, and $B_z = \pi/2$.

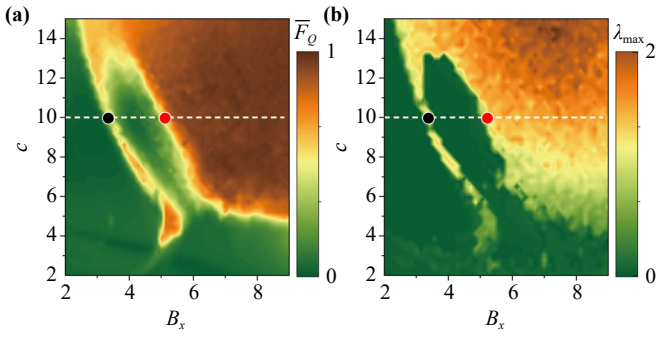

Fig. A6 **(a)** Rescaled time-averaged QFI $\overline{F}_Q$ and **(b)** MLE $\lambda_{\max}$ in the parameter space (B_x, c) with initial state R1, i.e., $|\theta,\phi\rangle_J = |0.33\pi, 0.9\pi\rangle$. Solid black and red points denote the pseudo-critical $(B_x = 3.3)$ and critical $(B_x = 5.3)$ points for entering the chaotic region when $c = 10$, respectively. We set $N = 200$ and $\tau = 100T$.

FOTOC for the initial states R1 and R2 (see Fig. 5), respectively.

To systematically characterize how chaotic transitions depend on nonlinearity, we map the phase boundary in the (B_x, c) parameter space using quantum $(\overline{F}_Q)$ and classical $(\lambda_{\max})$ measures, shown in Figs. A6(a) and (b), respectively. Both indicators consistently show that increasing c effectively lowers the critical driving amplitude B_x for entering the fully chaotic regime, offering an additional experimental control parameter to tune the chaos boundary.

Appendix E: Distributions of time-averaged QFI and FOTOC in fully chaotic regime

To visualize the FCS regime, we plot the distributions of $\overline{F}_Q$ and $\overline{C}$ in (S_z, ϕ) space for $B_x = 6.0$ — well above the critical value $B_x \approx 5.3$ (Fig. A7). Both quantities exhibit large, non-zero positive values across phase space, unlike the localized regular patterns formed by zero values in the MPS regime shown in Fig. 2(a) and Fig. 4(a). This striking contrast confirms the absence of regular islands and reflects global chaotic dynamics, consistent with the saturation of $\overline{C}$ observed in Fig. 5.

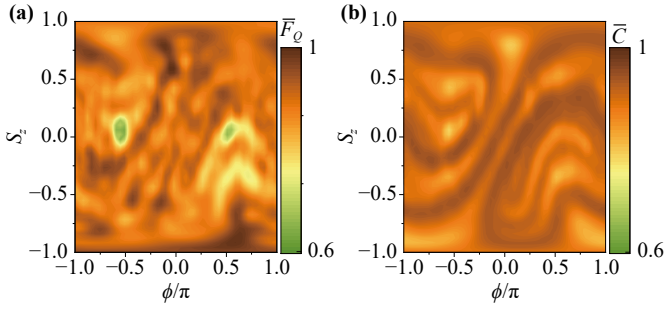

Fig. A7 Distributions of **(a)** rescaled time-averaged QFI $\overline{F}_Q$ and **(b)** time-averaged FOTOC $\overline{C}$ in the initial state space (S_z, ϕ) for the fully chaotic sea regime with driving strength $B_x = 6.0$. Parameters: $N = 200$, $\tau = 100T$, $B_z = \pi/2$, and $c = 10$.

References

1. R. V. Jensen, Quantum chaos, *Nature* 355(6358), 311 (1992)
2. S. Prants, Quantum–classical correspondence in chaotic dynamics of laser-driven atoms, *Phys. Scr.* 92(4), 044002 (2017)
3. A. Piga, M. Lewenstein, and J. Q. Quach, Quantum chaos and entanglement in ergodic and nonergodic systems, *Phys. Rev. E* 99(3), 032213 (2019)
4. E. J. Meier, J. Ang'ong'a, F. A. An, and B. Gadway, Exploring quantum signatures of chaos on a Floquet synthetic lattice, *Phys. Rev. A* 100(1), 013623 (2019)
5. C. J. Liu, Y. C. Meng, J. L. Qin, and L. Zhou, Classical and Quantum chaos in a spin-1 atomic Bose–Einstein condensate via Floquet driving, *Results Phys.* 43, 106091 (2022)
6. S. Chaudhury, A. Smith, B. Anderson, S. Ghose, and P. S. Jessen, Quantum signatures of chaos in a kicked top, *Nature* 461(7265), 768 (2009)
7. T. Olsacher, L. Pastori, C. Kokail, L. M. Sieberer, and P. Zoller, Digital quantum simulation. learning of the Floquet Hamiltonian.and quantum chaos of the kicked top, *J. Phys. A* 55(33), 334003 (2022)
8. L. Zhou and J. Gong, Floquet topological phases in a spin-1/2 double kicked rotor, *Phys. Rev. A* 97(6), 063603 (2018)
9. S. Tomsovic, J. D. Urbina, and K. Richter, Controlling quantum chaos: Time-dependent kicked rotor, *Phys. Rev. E* 108(4), 044202 (2023)
10. L. Zhou and J. Pan, Non-Hermitian Floquet topological phases in the double-kicked rotor, *Phys. Rev. A* 100(5), 053608 (2019)
11. R. Roncaglia, L. Bonci, F. M. Izrailev, B. J. West, and P. Grigolini, Tunneling versus chaos in the kicked harper model, *Phys. Rev. Lett.* 73(6), 802 (1994)
12. R. W. Bomantara, G. N. Raghava, L. Zhou, and J. Gong, Floquet topological semimetal phases of an extended kicked Harper model, *Phys. Rev. E* 93(2), 022209 (2016)
13. T. Zimmermann, H. D. Meyer, H. Köppel, and L. Cederbaum, Manifestation of classical chaos in the statistics of quantum energy levels, *Phys. Rev. A* 33(6), 4334 (1986)
14. J. Gómez, R. A. Molina, A. Relaño, and J. Retamosa, Misleading signatures of quantum chaos, *Phys. Rev. E* 66(3), 036209 (2002)
15. R. Aurich and F. Steiner, Statistical properties of highly excited quantum eigenstates of a strongly chaotic system, *Physica D* 64(1–3), 185 (1993)
16. Y. N. Zhou, T. G. Zhou, and P. Zhang, General properties of the spectral form factor in open quantum systems, *Front. Phys. (Beijing)* 19(3), 31202 (2024)
17. K. H. Song, Y. J. Zhao, Z. G. Shi, S. H. Xiang, and X. W. Chen, Scheme for n phase gates operation and one-

step preparation of highly entangled cluster state, *Eur. Phys. J. D* 66(1), 1 (2012)
18. H. L. Shi, A. Smerzi, and L. Pezzè, Quantum chaos, randomness and universal scaling of entanglement in various Krylov spaces, *SciPost Phys.* 19(4), 102 (2025)
19. P. M. Poggi and M. H. Muñoz-Arias, Measurement-induced multipartite-entanglement regimes in collective spin systems, *Quantum* 8, 1229 (2024)
20. R. Zheng, J. Qin, B. Chen, X. Zhao, and L. Zhou, Cavity-enhanced metrology in an atomic spin-1 Bose–Einstein condensate, *Front. Phys. (Beijing)* 19(3), 32204 (2024)
21. W. Liu, M. Zhuang, B. Zhu, J. Huang, and C. Lee, Quantum metrology via chaos in a driven Bose–Josephson system, *Phys. Rev. A* 103(2), 023309 (2021)
22. Q. Bin, L. L. Wan, F. Nori, Y. Wu, and X. Y. Lu¨, Out-of-time-order correlation as a witness for topological phase transitions, *Phys. Rev. B* 107(2), L020202 (2023)
23. S. Zamani, R. Jafari, and A. Langari, Out-of-time-order correlations and Floquet dynamical quantum phase transition, *Phys. Rev. B* 105(9), 094304 (2022)
24. Y. Huang, Y. L. Zhang, and X. Chen, Out-of-time-ordered correlators in many-body localized systems, *Ann. Phys.* 529(7), 1600318 (2017)
25. C. J. Lin and O. I. Motrunich, Out-of-time-ordered correlators in a quantum Ising chain, *Phys. Rev. B* 97(14), 144304 (2018)
26. T. Yoshimura, S. J. Garratt, and J. Chalker, Operator dynamics in Floquet many-body systems, *Phys. Rev. B* 111(9), 094316 (2025)
27. D. A. Roberts, D. Stanford, and L. Susskind, Localized shocks, *J. High Energy Phys.* 2015(3), 51 (2015)
28. B. Yan, L. Cincio, and W. H. Zurek, Information scrambling and Loschmidt echo, *Phys. Rev. Lett.* 124(16), 160603 (2020)
29. F. Meier, M. Steinhuber, J. D. Urbina, D. Waltner, and T. Guhr, Signatures of the interplay between chaos and local criticality on the dynamics of scrambling in many-body systems, *Phys. Rev. E* 107(5), 054202 (2023)
30. M. Gärttner, J. G. Bohnet, A. Safavi-Naini, M. L. Wall, J. J. Bollinger, and A. M. Rey, Measuring out-of-time-order correlations and multiple quantum spectra in a trapped-ion quantum magnet, *Nat. Phys.* 13(8), 781 (2017)
31. J. Li, R. Fan, H. Wang, B. Ye, B. Zeng, H. Zhai, X. Peng, and J. Du, Measuring out-of-time-order correlators on a nuclear magnetic resonance quantum simulator, *Phys. Rev. X* 7(3), 031011 (2017)
32. E. B. Rozenbaum, S. Ganeshan, and V. Galitski, Lyapunov exponent and out-of-time-ordered correlator's growth rate in a chaotic system, *Phys. Rev. Lett.* 118(8), 086801 (2017)
33. J. Rammensee, J. D. Urbina, and K. Richter, Many-body quantum interference and the saturation of out-of-time-order correlators, *Phys. Rev. Lett.* 121(12), 124101 (2018)
34. J. Maldacena, S. H. Shenker, and D. Stanford, A bound on chaos, *J. High Energy Phys.* 2016(8), 106 (2016)
35. R. Kidd, A. Safavi-Naini, and J. Corney, Saddle-point scrambling without thermalization, *Phys. Rev. A* 103(3), 033304 (2021)
36. I. C. Percival, Regular and irregular spectra, *J. Phys. B* 6(9), L229 (1973)
37. G. He, B. Ye, R. Gong, Z. Liu, K. W. Murch, N. Y. Yao, and C. Zu, Quasi-Floquet prethermalization in a disordered dipolar spin ensemble in diamond, *Phys. Rev. Lett.* 131(13), 130401 (2023)
38. T. Zibold, E. Nicklas, C. Gross, and M. K. Oberthaler, Classical bifurcation at the transition from Rabi to Josephson dynamics, *Phys. Rev. Lett.* 105(20), 204101 (2010)
39. M. Steel, and M. Collett, Quantum state of two trapped Bose-Einstein condensates with a Josephson coupling, *Phys. Rev. A* 57(4), 2920 (1998)
40. B. Wu, and J. Liu, Commutability between the semiclassical and adiabatic limits, *Phys. Rev. Lett.* 96(2), 020405 (2006)
41. P. Hauke, M. Heyl, L. Tagliacozzo, and P. Zoller, Measuring multipartite entanglement through dynamic susceptibilities, *Nat. Phys.* 12(8), 778 (2016)
42. S. C. Li, L. Pezzè, and A. Smerzi, Multiparticle entanglement dynamics of quantum chaos in a Bose–Einstein condensate, *Phys. Rev. A* 103(5), 052417 (2021)
43. L. Pezzè, A. Smerzi, M. K. Oberthaler, R. Schmied, and P. Treutlein, Quantum metrology with nonclassical states of atomic ensembles, *Rev. Mod. Phys.* 90(3), 035005 (2018)
44. A. Smerzi, A. Trombettoni, T. Lopez-Arias, C. Fort, P. Maddaloni, F. Minardi, and M. Inguscio, Macroscopic oscillations between two weakly coupled Bose–Einstein condensates, *Eur. Phys. J. B* 31(4), 457 (2003)
45. M. Albiez, R. Gati, J. Fölling, S. Hunsmann, M. Cristiani, and M. K. Oberthaler, Direct observation of tunneling and nonlinear self-trapping in a single bosonic Josephson junction, *Phys. Rev. Lett.* 95(1), 010402 (2005)
46. W. Wu and J. H. An, Gaussian quantum metrology in a dissipative environment, *Phys. Rev. A* 104(4), 042609 (2021)
47. U. Alushi, A. Coppo, V. Brosco, R. Di Candia, and S. Felicetti, Collective quantum enhancement in critical quantum sensing, *Commun. Phys.* 8(1), 74 (2025)
48. S. Pilatowsky-Cameo, J. Chávez-Carlos, M. A. Bastarrachea-Magnani, P. Stránskỳ, S. Lerma-Hernández, L. F. Santos, and J. G. Hirsch, Positive quantum Lyapunov exponents in experimental systems with a regular classical limit, *Phys. Rev. E* 101(1), 010202 (2020)
49. D. Marković and M. Čubrović, Detecting few-body quantum chaos: Out-of-time ordered correlators at saturation, *J. High Energy Phys.* 2022(5), 23 (2022)
50. P. Blocher, S. Asaad, V. Mourik, M. Johnson, A. Morello, and K. Mølmer, Measuring out-of-time-ordered correlation functions without reversing time evolution, *Phys. Rev. A* 106(4), 042429 (2022)
51. B. Swingle, G. Bentsen, M. Schleier-Smith, and P. Hayden, Measuring the scrambling of quantum information, *Phys. Rev. A* 94(4), 040302 (2016)
52. D. Hall, M. Matthews, J. Ensher, C. Wieman, and E. A. Cornell, Dynamics of component separation in a binary mixture of Bose–Einstein condensates, *Phys. Rev. Lett.* 81(8), 1539 (1998)

53. C. Lee, J. Huang, H. Deng, H. Dai, and J. Xu, Nonlinear quantum interferometry with Bose condensed atoms, *Front. Phys. (Beijing)* 7(1), 109 (2012)
54. C. Gross, T. Zibold, E. Nicklas, J. Esteve, and M. K. Oberthaler, Nonlinear atom interferometer surpasses classical precision limit, *Nature* 464(7292), 1165 (2010)
55. S. Kotochigova, Controlling interactions between highly magnetic atoms with Feshbach resonances, *Rep. Prog. Phys.* 77(9), 093901 (2014)
56. V. Mourik, S. Asaad, H. Firgau, J. J. Pla, C. Holmes, G. J. Milburn, J. C. McCallum, and A. Morello, Exploring quantum chaos with a single nuclear spin, *Phys. Rev. E* 98(4), 042206 (2018)